Supplement to **"Online and offline decoding of continuous limb movements from high-density epidural electrode arrays using custom spatial filters"**

A.R. Marathe, & D.M. Taylor

***Array manufacturing details*:** Arrays were made with seven-stranded, stainless steel, Teflon-coated wires (#793500 A-M Systems; 0.0002 inch combined wire diameter not including insulation) embedded in a methyl methacrylate base. In monkey I, the wires were cut flush with the bottom of the methyl methacrylate base. Therefore, the contact area was limited to the cross-sectional cut area of the multistranded wire. In monkey II, the multistranded wire extended through the methyl methacrylate base, laid flat against the base for about 2 mm, and then looped back into the base. Therefore, the contact area for each electrode consisted of a ~2 mm long section of the outer surface of the multistranded wire. After several months, monkey II's first epidural electrode array started to come loose and was replaced by a third design that also had ~2mm of exposed deinsulated wire. However, this time the multistranded wire was splayed apart for more surface area and located within a 0.027 inch diameter channel within the methyl methacrylate base thus allowing more electrode-to-fluid surface contact. Average impedance measures for each type of electrode were approximately 17 kΩ for monkey I and 10 kΩ for monkey II's first electrode and 3 kΩ for the replacement electrode when measured at 1KHz relative to a nearby de-insulated wire ground. Channels with impedances > 500 kΩ or that had large intermittent changes in amplitude indicative of an unstable connection were considered faulty and not included in the average impedance values or data analysis. Figure S1 below shows example raw traces along with spatially-filtered versions of the same data.

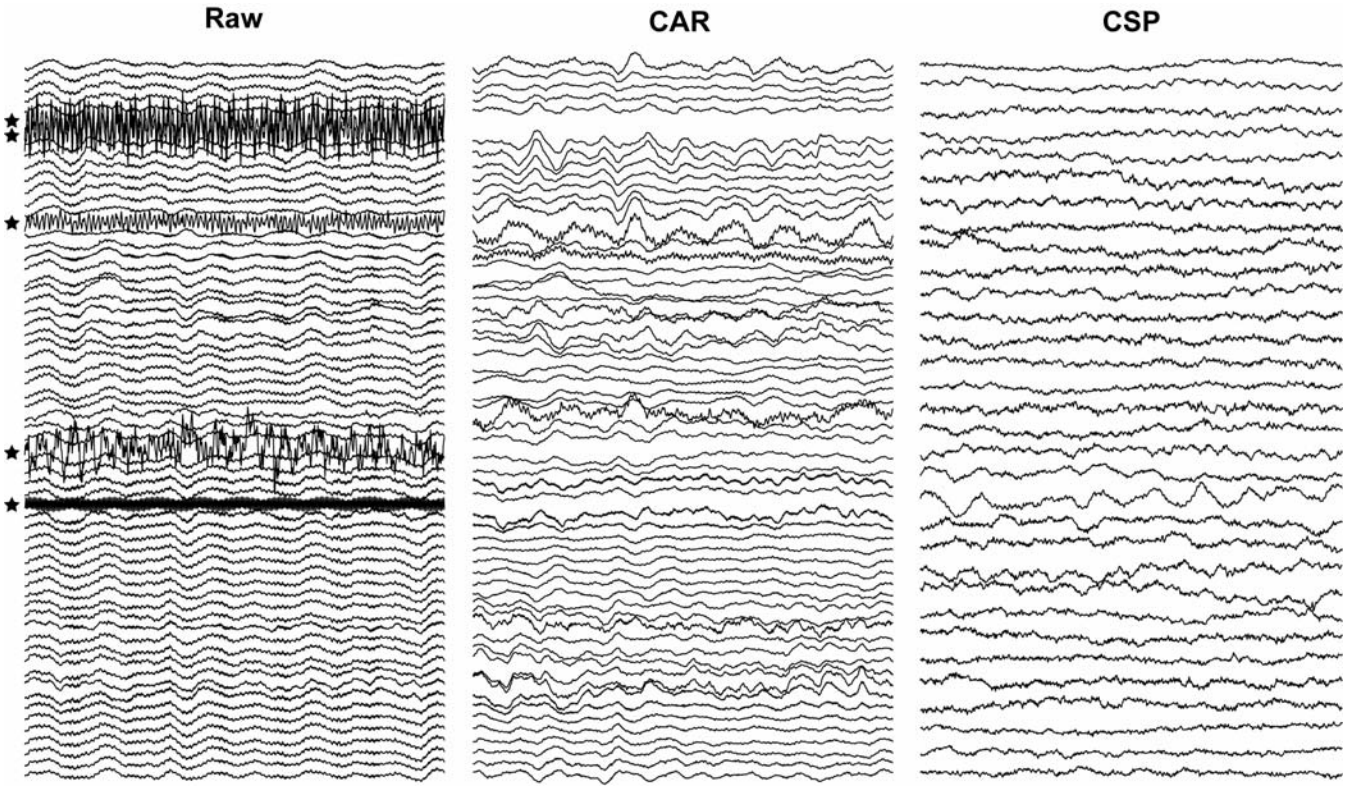

Figure S1: Examples of raw and spatially-filtered epidural field potentials. The example traces on the left show the 64 raw field potentials from Monkey I. The five channels marked with stars were deemed defective and removed for all further data analysis. The middle column shows the common averaged referenced (CAR) traces from the remaining 59 signals. The right column contains the top-ranked 32 CSP-filtered signals from the same raw data (CSP Cardinal, 67% removed).

Figure S2 below shows an example of the movement-related changes in the power bands used for 2D movement decoding. In addition to the expected movement-related desynchronization in the alpha and beta bands and an increase in power in the gamma range, the plots in figure S2B show that movements to different corners of the workspace resulted in additional band-specific changes that could have been utilized by the decoders to predict 2D movement.

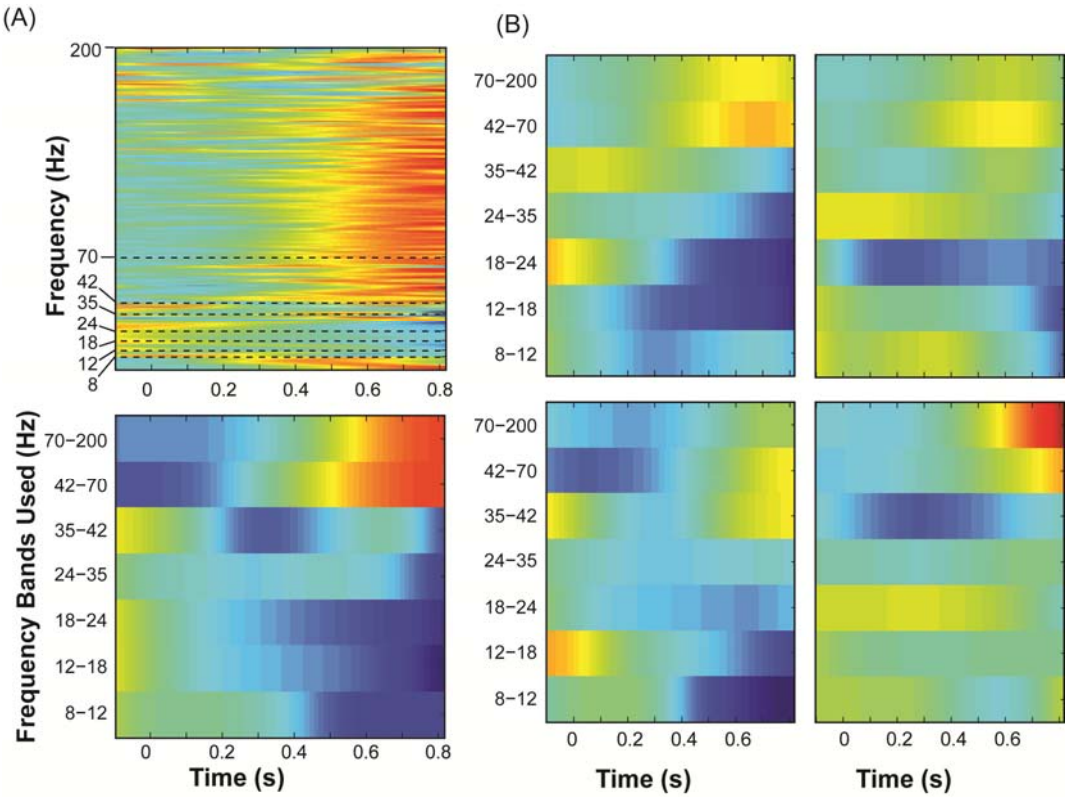

Figure S2: Examples of movement-related spectrograms from the raw epidural field potentials. Individual power bands were z-scored. Red indicates the highest power level and dark blue indicates the lowest power level: A) Spectrograms averaged across all center-out trials. Top plot includes all frequencies; bottom plot shows mean power values in the frequency bands used for decoding). B) The same spectrogram data shown in the bottom of (A) but averaged separately for movements to each of the four targets. Plot arrangement indicates movement direction (e.g. bottom left plot is for movements to a bottom left target).

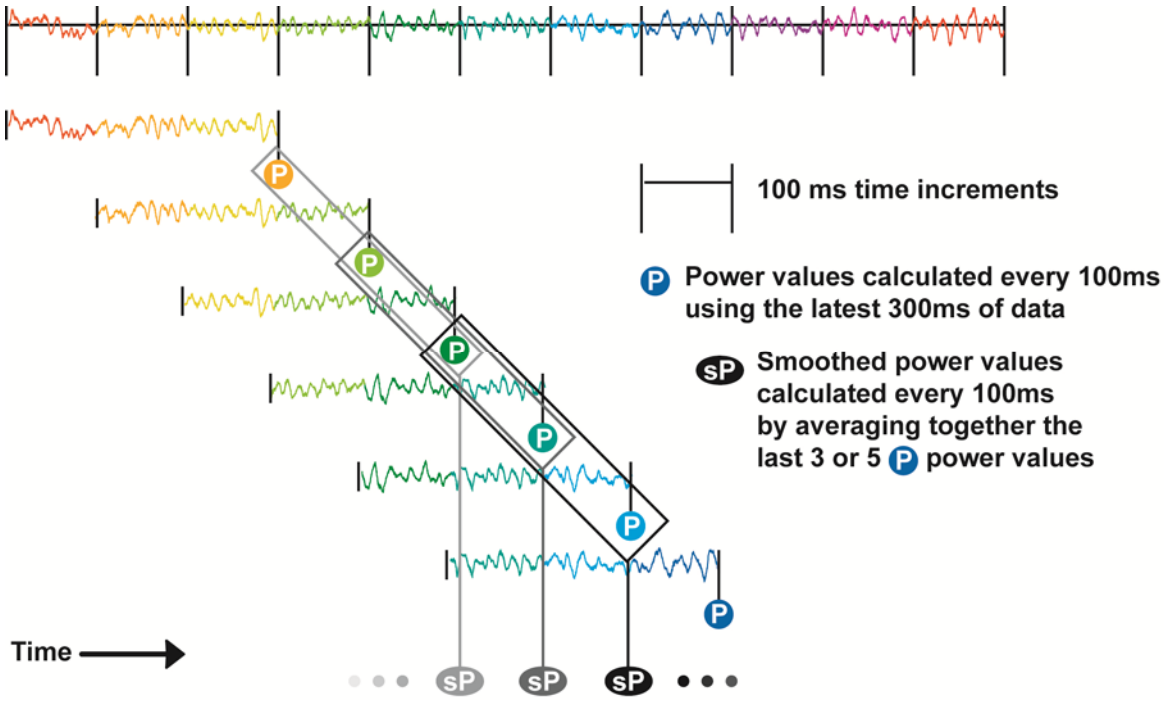

Figure S3: Diagram illustrating how power data was initially calculated and then smoothed. Data was parsed for calculating power (P) every 100ms using the latest 300 ms of raw signals. Those power calculations were either used 'as is' or further smoothed (sP) by averaging together the latest three or five power calculations. Each diagonal rectangle signifies smoothing over three power values in the diagram above.

Full continuous wrist position decoding results are shown below in figure S4 (linear regression decoding) and figure S5 (Kalman filter decoding). Plot colors represent the mean coefficient of determination, R^2, calculated between the actual and predicted continuous wrist position values. Means were calculated by averaging R^2 values for the *X* and *Y* components of movements from all ten cross-validation testing sets and all 64 recording sessions. R^2 accuracy measures are plotted separately for each filter type as a function of each level of power smoothing (i.e. power values averaged across one (no smoothing), three, or five consecutive 100ms time bins) and each number of spatially-filtered signals used (4, 8, 12, 16, and 32). Data was linearly interpolated between these points to illustrate the change in accuracy trends across the parameter space.

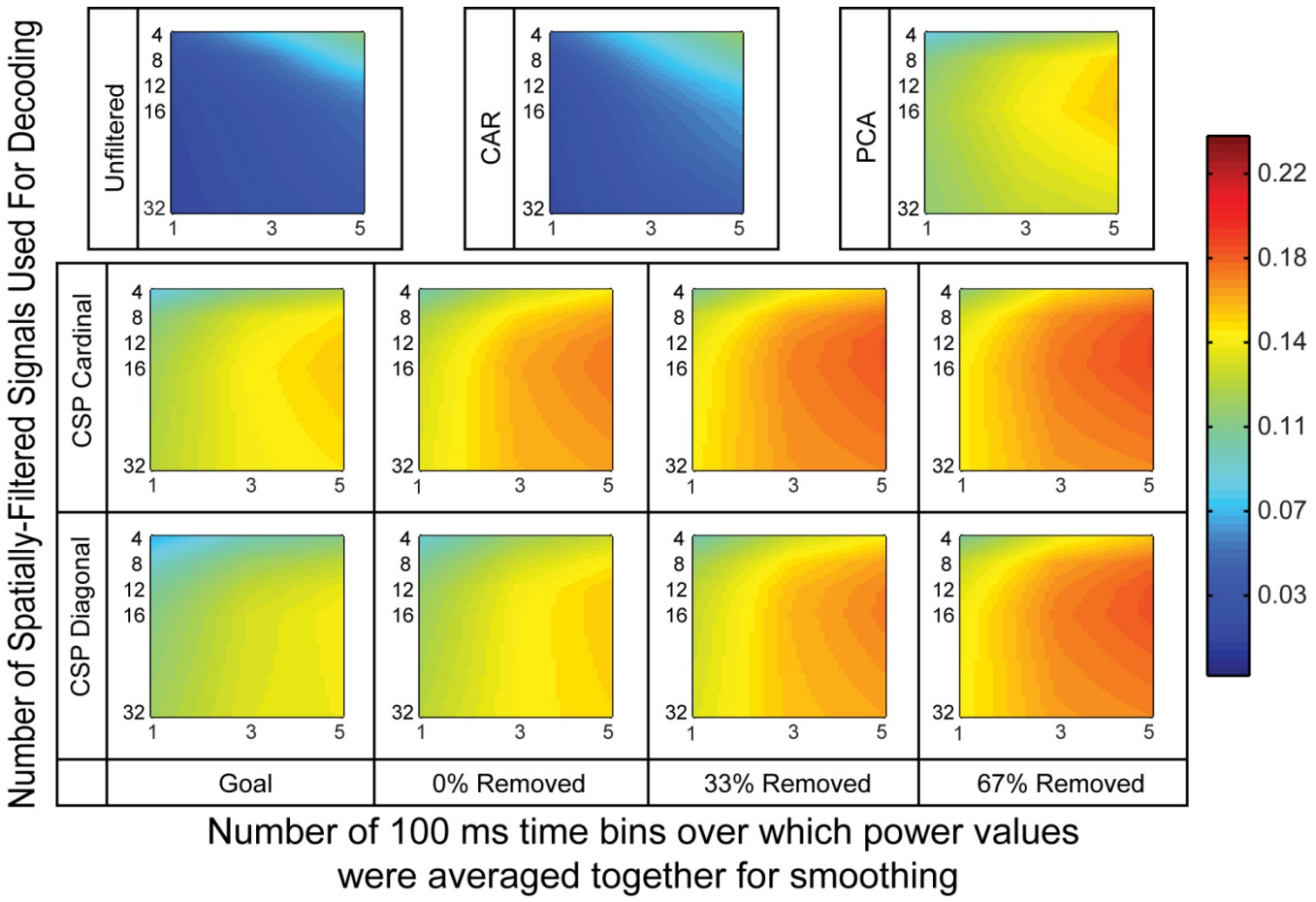

Figure S4: Average linear regression wrist position decoding performance as measured by the mean coefficient of determination, R^2.

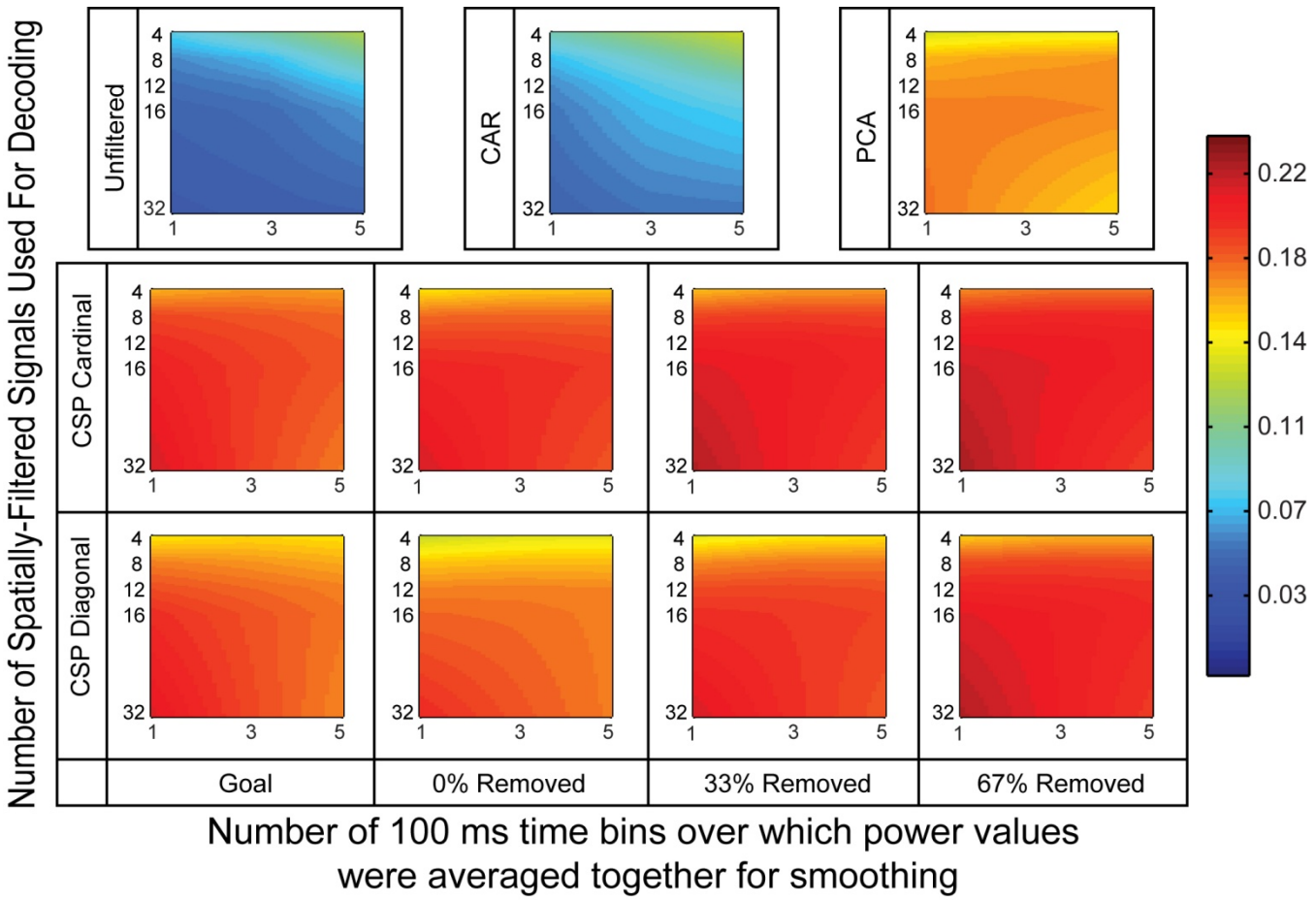

Figure S5: Average Kalman filter wrist position decoding performance as measured by the mean coefficient of determination, R^2.

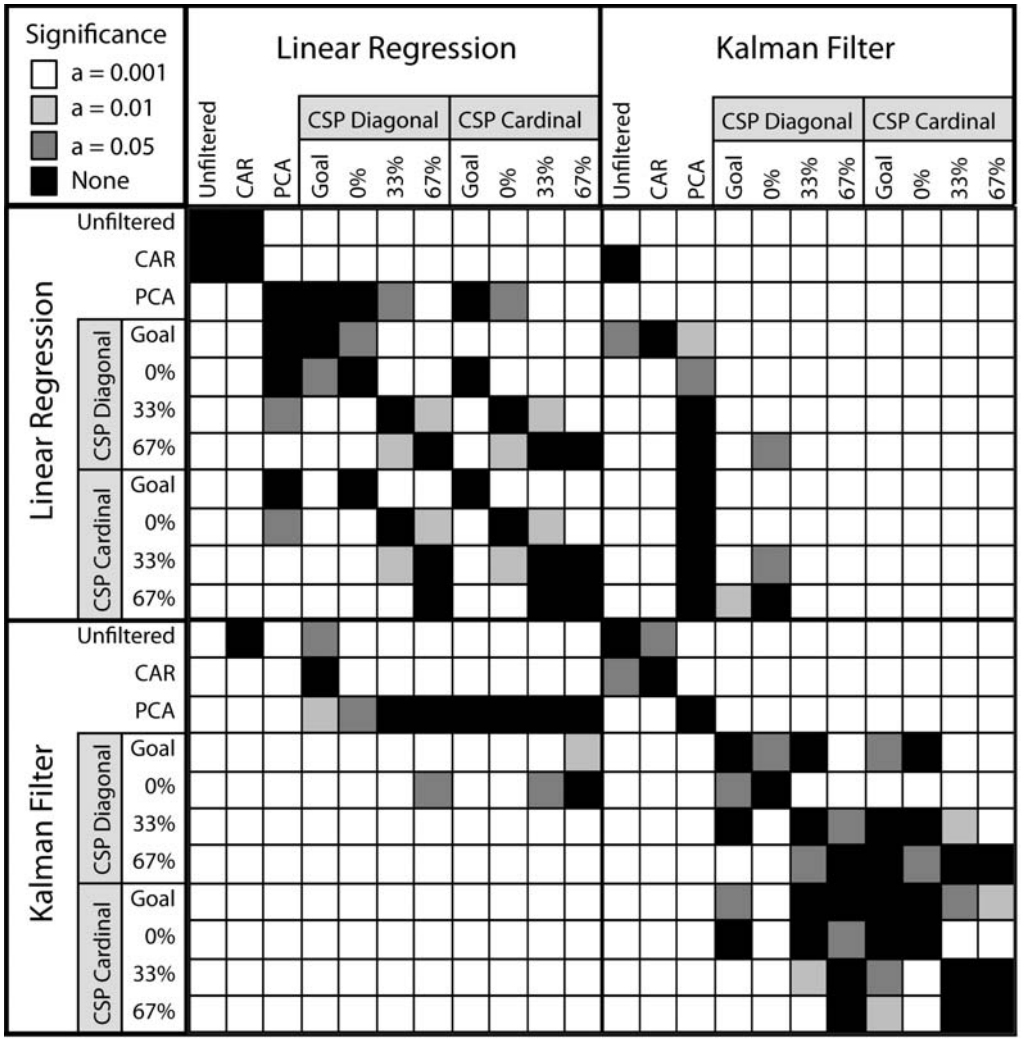

Figure S6: Statistical comparison of the decoding accuracy of all pairs of spatial filter and decoder options. Each decoder/filter combination was individually optimized for the amount of temporal smoothing and the number of filtered signals used. Shading indicates the degree of statistical significance of the differences in decoder performance (R^2) between each pair of optimized options as measured using the Wilcoxon Sign Rank test**.** White squares indicate a significant difference at $\alpha = 0.001$. Light gray squares indicate a significant difference at $\alpha = 0.01$. Dark gray squares indicate a significant difference at $\alpha = 0.05$. Black squares indicate that results were not significant at $\alpha = 0.05$ or smaller.

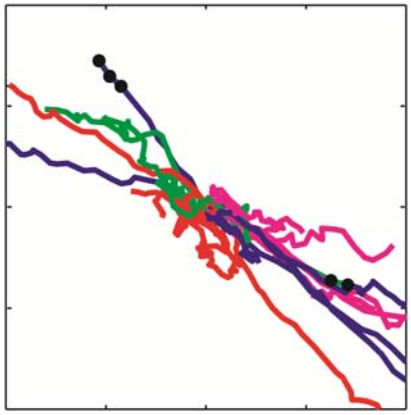

Figure S7: Closed-loop center-out trajectories when decoded wrist velocity was used to control the velocity of the cursor in real time. Black dots indicate when the correct target was hit. Trajectories were color coded by intended target as in figure 6 in the main text. Only three blocks were collected as the animal got frustrated and stopped trying after that.

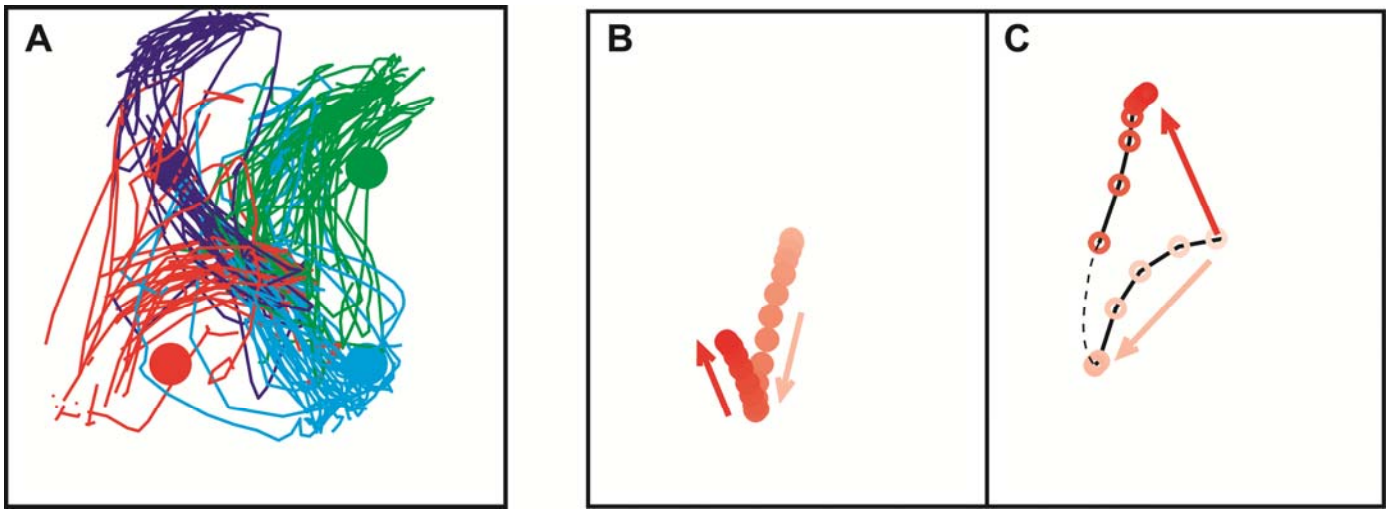

Figure S8: Hand trajectories recorded during the brain-control task where decoded hand position controlled cursor velocity. Trajectories are color coded by intended target. Target locations are indicated by large dots. Gaps in the trajectories are where the position sensor went out of view of the motion capture system. All hand trajectories are plotted together in (A). The concept of the position-to-velocity mapping is illustrated in (B & C) by an example where the animal corrected a trajectory error online. (B) shows a brain-controlled cursor path to the bottom left target and (C) shows the associated hand path (dotted line estimates the path where the position sensor was out of view). In this example, hand positions in the first half of the trial were mainly in the bottom left part of the workspace relative to the center (0,0) neutral position as shown by the lighter red arrow in (C). The associated neural signals were decoded and mapped to down and leftward incremental changes in cursor position at each timestep (i.e. Δposition/Δtime or velocity) as indicated by the lighter red arrow in (B). However, this brain-controlled trajectory still missed the intended target and needed to be redirected up and to the left. Therefore, part way through the trial, the animal moved its hand to an upper left position in the workspace for the last part of the trial (as indicated by the darker red arrow pointing to overlapping hand positions at the end of the movement in (C)). These up and left hand positions were mapped to up and leftward cursor velocity values (dark red arrow in B), which successfully redirected the cursor to the desired target location.